Acta Materialia 303 (2026) 121701

Contents lists available at ScienceDirect

Acta Materialia

journal homepage: www.elsevier.com/locate/actamat

Manipulating the electronic structure of bismuth oxide by selenium incorporation for efficient and reversible zinc-ion storage

Jian Xu [a,1], Jingchen Zhang [b,1], Zeyu Hao [a,1], Xiliang Gong [c], Zeshuo Meng [a], Yutong Zhao [a], Shulong Wang [a], Haoteng Sun [d,*], Hongwei Tian [a,*], Dawei Su [e,*]

[a] Key Laboratory of Automobile Materials MOE, School of Materials & Engineering, Jilin Provincial International Cooperation Key Laboratory of High-Efficiency Clean Energy Materials, Jilin University, Changchun 130012, China
[b] Institute for Physical Science and Technology, University of Maryland, College Park, MD, 20742, United States
[c] Department of Chemistry and Biochemistry, University of Maryland, College Park, MD, 20742, United States
[d] Department of Chemistry, Brown University, RI 02912, United States
[e] Applied Chemistry and Environment Science, School of Science, STEM College, RMIT University, Melbourne VIC 3000, Australia

ARTICLE INFO

Keywords:
Bismuth oxide
Selenium incorporation
Zinc-ion batteries
Electronic structure engineering
Chemical vapor deposition

ABSTRACT

Bismuth oxide, with its large internal spaces and adjustable structures, is a promising electrode material for zinc-ion batteries (ZIBs). However, its application is limited by poor reversibility and rapid capacity fading in neutral zinc-ion electrolytes. Here, we introduce selenium into bismuth oxide using chemical vapor deposition, precisely controlling the Se content by adjusting the gas flow rate. The Se-doped materials, particularly CC/$Bi_2O_{2.5}Se_{0.5}$ and CC/Bi_2O_2Se, exhibit significant improvements in specific capacity and cycling stability. CC/Bi_2O_2Se achieves a maximum specific capacity of 312.5 mAh g^{-1} at 0.1 A g^{-1}, with a retention rate of 74.6 % after 4000 cycles at 2 A g^{-1}. The enhanced performance is attributed to the narrowed band gap and improved electrical conductivity resulting from Se doping, which facilitates electron and ion transport. More importantly, Se incorporation mitigates the formation of detrimental by-products, ensuring more reversible and efficient Zn-ion storage. It also stabilizes the Bi^{3+}↔Bi° conversion pathway observed during cycling, providing a metal-centered rationale for the improved reversibility. This work highlights the importance of electronic structure regulation in optimizing the performance of metal oxide electrodes and provides valuable insights for the rational design of high-performance energy storage materials.

1. Introduction

Aqueous electrochemical energy storage devices based on zinc ion systems, such as zinc-ion batteries and zinc-ion capacitors, utilize zinc metal as the anode, thereby achieving high theoretical capacity, well-balanced kinetic properties, and excellent reaction reversibility. Consequently, these devices exhibit high specific capacity and energy density [1,2]. Especially for zinc-ion batteries utilizing neutral electrolytes, compared to alkaline systems, the zinc anode encounters less severe corrosion and side reactions [3], which makes neutral $ZnSO_4$-based media more relevant to practical Zn||oxide full cells. Due to the large ionic radius of hydrated zinc ions (5.5 Å) [4], the electrode needs to have an appropriate structure and sufficient internal space to ensure the migration of zinc ions. Bismuth oxide generally has large internal spaces and adjustable structures [5]. However, most studies on Bi_2O_3 electrode materials have been conducted in alkaline electrolytes (e.g., KOH), where high capacity and rate capability are typically reported [6–8]; yet such alkaline media are intrinsically incompatible with a Zn metal anode because of severe corrosion and parasitic reactions. As a result, there remain few investigations of Bi_2O_3 in neutral Zn-ion systems, despite their higher relevance to practical devices.

Previously, Bi_2O_3 indeed exhibited high specific capacity and rate performance in alkaline zinc-ion batteries [6–8]; however, when paired with neutral electrolytes such as $Zn(CF_3SO_3)_2$ or $ZnSO_4$, its capacity rapidly declines to below 50 mAh g^{-1} within only a few cycles and the storage mechanism remains ambiguous [9]. Possible pathways include a conversion reaction (Bi_2O_3 ↔ Bi) or Zn^{2+}/H^+ intercalation–deintercalation, analogous to those reported for bismuth

* Corresponding authors.
E-mail addresses: haoteng_sun@brown.edu (H. Sun), tianhw@jlu.edu.cn (H. Tian), dawei.su@rmit.edu.au (D. Su).
[1] These authors contributed equally to this work.

https://doi.org/10.1016/j.actamat.2025.121701
Received 30 June 2025; Received in revised form 9 October 2025; Accepted 4 November 2025
Available online 5 November 2025

chalcogenides such as Bi_2Se_3 [10] and Bi_2Te_3 [11]. In neutral $ZnSO_4$, the poor reversibility of Bi_2O_3 is associated with strong Zn^{2+}–O^{2-} electrostatic interaction within the oxide lattice and with the lower ionic/electronic conductivity of the Bi_2O_3/neutral-electrolyte pair, which together promote ZHS by-products and sluggish charge/ion transport [12]. Therefore, it is essential to regulate the structure and electronic characteristics of Bi_2O_3 to achieve efficient and reversible Zn-ion storage in $ZnSO_4$ electrolyte [13,14], in particular, by stabilizing the metal-centered $Bi^{3+}\leftrightarrow Bi^{\circ}$ conversion under neutral conditions—a motivation that directly frames our subsequent Se-incorporation strategy.

For bismuth oxide electrode materials, selenium (Se) doping or introducing Se into the structure is an efficient storage strategy that can effectively regulate their electronic structure to achieve zinc ions. Se has a larger atomic radius (1.6 Å) and lower electronegativity than O and S [15]. The chemical bond between metal and selenium exhibits higher covalency compared to the metal-oxygen bond, which facilitates better electronic conductivity and enhances charge transport. In this context, tuning Bi–Se metal–anion covalency also facilitates a more reversible $Bi^{3+}\leftrightarrow Bi^{\circ}$ conversion, linking electronic-structure regulation to the observed cycling stability. Therefore, introducing Se into metal oxide materials can enhance their intrinsic electrical conductivity by narrowing the band gap, thereby improving the electrochemical activity of the electrodes [16]. Furthermore, from the perspective of chemical bonds, introducing Se can effectively modulate the strength of the metal-oxygen ($M-O$) bond. This modulation significantly influences the reconstruction or transformation reactions of the material during the electrochemical process [17]. Additionally, it reduces the electrostatic interaction between O^{2-} in the metal oxide structure and Zn^{2+} in the electrolyte, thereby preventing rapid capacity fading of the material. Especially for Bi_2O_3 materials, since their electrochemical energy storage mechanism mainly relies on the Faraday process, an overly strong interaction between the structure and Zn^{2+} ions would be detrimental to the mass transfer during the electrochemical reaction process. Therefore, the introduction of Se can optimize the structural regulation of Bi_2O_3 and enhance its energy storage performance [18,19]. Notably, our previous study showed that constructing a Bi−interlayer/NiCoP heterostructure (featuring a built-in electric field that synergistically accelerates electron and ion transport) yielded a high specific capacitance of 1200 F g^{-1} and an energy density of 319.1 Wh kg^{-1} in aqueous energy-storage devices [20]. This interfacial-engineering paradigm provides critical guidance for the present work, which further tunes the electronic structure of Bi_2O_3 by means of Se doping.

In the synthesis process of introducing Se into the bismuth oxide structure, selecting an appropriate doping or introduction method is crucial. Vapor deposition technology can precisely control the composition of the doped material while preserving the original structure. Compared to traditional wet chemical methods, vapor deposition reduces reliance on organic solvents, resulting in a simpler, more efficient, and environmentally friendly reaction process [21]. The final products obtained through chemical vapor deposition (CVD) for doping or material structure regulation are closely influenced by several key parameters: (i) the type and quality of reactants and precursors, (ii) substrate engineering, (iii) reaction temperature, and (iv) gas flow rate [22,23]. Many previous studies have also employed CVD to sulfide or selenide transition metal-based materials [24–26]. However, these studies uniformly controlled product formation by adjusting the mass of S powder or Se powder used in the reaction. Compared with regulating the mass of Se powder, adjusting the gas flow rate in the reaction chamber can enhance the uniformity of the precursor surface reactions and precisely control the Se supply. This approach effectively avoids side reactions and resource waste associated with excessive Se powder. Therefore, by adjusting the gas flow rate CVD to introduce Se into bismuth oxides, different products can be obtained. Analyzing the deposition process, product structure, and their electrochemical performance helps understand the correlation between reaction conditions, product structure, and electrochemical performance. This provides crucial theoretical and experimental insights for future precise or large-scale preparation of electrode materials.

In this study, a series of bismuth-based compound electrodes with varying degrees of Se doping were successfully synthesized using the CVD method. The precursors were characterized, and COMSOL simulations were employed to investigate the relationship between gas flow rate and the obtained products, thereby elucidating the Se incorporation process in bismuth oxide materials. Through systematic characterization and in-depth analysis of the electrochemical processes, we elucidated the energy storage mechanism of the conversion reaction of Bi_2O_3 in $ZnSO_4$ electrolyte ($Bi_2O_3 \leftrightarrow Bi$). Additionally, we investigated the factors contributing to its low specific capacity and rapid capacity fade. This phenomenon stems from the strong interaction between the electronic structure of bismuth oxide and Zn^{2+}, which leads to a large amount of basic zinc sulfate ($Zn_4(OH)_6SO_4{\cdot}4H_2O$, ZHS) by-products adhering to the electrode surface, hindering the ion transport in the conversion reaction and preventing the reaction from proceeding reversibly and continuously [27]. By introducing selenium to modulate the electronic structure of bismuth oxide, the internal electron transport and zinc ion diffusion within the material were enhanced. This approach mitigated the adverse effects of ZHS on mass transfer during electrochemical reactions, thereby achieving high specific capacity and prolonged cycling stability of the electrode in $ZnSO_4$ electrolyte.

2. Experimental methods

2.1. Materials

Bismuth nitrate ($Bi(NO_3)_3{\bullet}5H_2O$), ammonium iodide (NH_4I), nitric acid (HNO_3), p-benzoquinone ($C_6H_4O_2$), anhydrous ethanol (C_2H_5OH), sodium borohydride ($NaBH_4$), sodium hydroxide (NaOH) and selenium powder (Se) were purchased from Aladdin Industrial Corporation. The chemicals were of analytical grade and used as received without further purification. The carbon cloth (CC) substrate (W0S1011) used in this study was procured from Ce Tech Co., Ltd.

2.2. Preparation of precursors

As shown in Scheme 1, we first electrodeposit BiOI on carbon cloth (CC), then convert it to the CC/Bi–BiO_x precursor by treatment in $NaBH_4$ solution, followed by selenylation under Ar to obtain the final products. First, 2 mmol of $Bi(NO_3)_3{\cdot}5H_2O$ and 10 mmol of NH_4I were dissolved in 50 mL of deionized water under continuous stirring. The solution was then acidified by slowly adding 0.5 M nitric acid until the pH reached 1.7. Next, 20 mL of a 0.23 M p-benzoquinone ethanol solution was added to the mixture, followed by magnetic stirring for 30 min to ensure thorough mixing. During the electrodeposition process, a carbon cloth with an area of 1 cm^2 served as the working electrode, a platinum sheet as the counter electrode, and an Ag/AgCl electrode as the reference electrode. The electrochemical cell was configured in a three-electrode system. Constant potential deposition was performed at −0.1 V for 200 s. Upon completion of the electro-deposition process, the samples were sequentially washed with water and ethanol, followed by vacuum drying to yield CC/BiOI. Subsequently, the CC/BiOI electrode was immersed in a 0.23 M $NaBH_4$ solution for 20 min, after which it was thoroughly rinsed with deionized water and vacuum-dried to obtain the precursor.

2.3. Preparation of CC/Bi_2O_3 and Se-doped bismuth-based compound electrodes

The precursor was placed in a tube furnace and annealed at 300 °C for 2 h under an Ar atmosphere to obtain the CC/Bi_2O_3 electrode. Using the same annealing conditions, 60 mg of Se powder was positioned 10 cm upstream from the precursor. By controlling the gas flow rate,

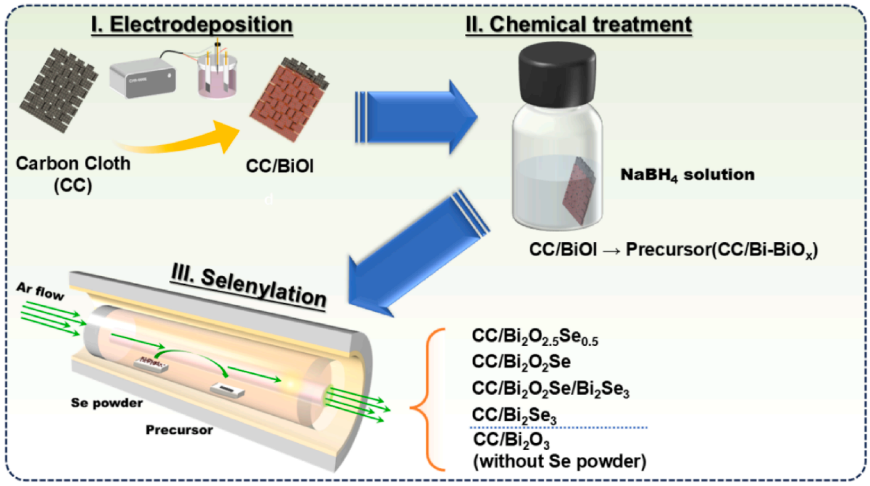

Scheme 1. Schematic illustration of the synthesis workflow.

different products were synthesized. When the gas flow rate was 30 mL min^{-1}, the final sample obtained was a Se-doped Bi_2O_3 electrode, denoted as CC/$Bi_2O_{2.5}Se_{0.5}$ based on the Se content. At a gas flow rate of 60 mL min^{-1}, a bismuth selenide oxide electrode (CC/Bi_2O_2Se) was formed. When the gas flow rate increased to 90 mL min^{-1}, a mixed phase of Bi_2O_2Se and Bi_2Se_3 (CC/Bi_2O_2Se-Bi_2Se_3) was synthesized. For gas flow rates of 120 mL min^{-1} or higher, a pure Bi_2Se_3 phase (CC/Bi_2Se_3) was obtained (see Fig. S3b). The mass of the active material loaded on each electrode was approximately 1 to 1.5 mg.

2.4. Materials characterization

The phase and crystal structure of the samples were analyzed by X-ray diffraction (XRD, D8-Advances, CuKα radiation, λ = 1.5406 Å). The composition of the material was further analyzed by Raman spectroscopy (HORIBA HR800). The morphology of the samples was characterized by scanning electron microscopy (SEM, Hitachi SU8010) and transmission electron microscopy (TEM, JEOL JEM-2200FS). The elemental distribution of the samples was analyzed by energy-dispersive spectroscopy (EDS). The surface chemical state of the material was detected by X-ray photoelectron spectroscopy (XPS, ESCALAB-250, AlKα radiation). The absorbance spectra were collected using a UV–vis diffuse reflectance spectrometer (Shimadzu, model UV-3600). The electrical conductivity of the electrode sheets was measured using a four-probe conductivity meter (Bolun Jingwei, model ST-2235).

2.5. Electrochemical measurement

The zinc-ion battery consists of a bismuth-based cathode and a zinc foil anode, using 1 M $ZnSO_4$ solution as the electrolyte. Cyclic voltammetry (CV), galvanostatic charge-discharge (GCD), and electrochemical impedance spectroscopy (EIS) measurements were conducted using a CHI 760e workstation from Shanghai Chenhua Instrument Co., Ltd. Cyclic stability tests and galvanostatic intermittent titration technique (GITT) measurements were conducted using the Land battery testing system (CT2001A). All specific capacities were normalized to the mass of the as-formed active phase (Bi_2O_3, $Bi_2O_{2.5}Se_{0.5}$, or Bi_2O_2Se) on carbon cloth, excluding the substrate. The active mass was determined by weighing the carbon cloth before and after growth/treatment on the same microbalance (dry state).

3. Results and discussion

3.1. Characterization of precursors and analysis of the vapor deposition process

The phase of the precursor was characterized by XRD (Fig. 1a). Diffraction peaks were observed at 27.16°, 37.96°, 39.62°, and 48.70°, corresponding to the hexagonal crystal structure of metal Bi (PDF card No 96–006–4703). No diffraction peaks attributable to BiOI or Bi_2O_3 crystals were detected. This indicates that after reduction treatment with $NaBH_4$ solution, a portion of BiOI has been successfully transformed into metal Bi. In the Fourier transform infrared (FTIR) spectrum (Fig. 1b), broad peaks observed at 747 and 897 cm^{-1} are indicative of the presence of Bi−*O* bonds [28]. Through XPS analysis, we examined the surface chemical composition and oxidation states of the precursor. The full scan (Fig. S1a) indicate that the sample consists solely of Bi, O, and C, with no detectable I or other elements. The significant presence of oxygen suggests that a portion of bismuth may be present in the form of oxides. However, due to the low crystallinity, the corresponding diffraction peaks for these oxides are not observable in the XRD pattern. Based on the spectrum of the Bi 4f in Fig. 1c, characteristic peaks corresponding to the Bi-Bi bond were observed at 156.9 and 162.3 eV. Additionally, peaks at 159.1 and 164.4 eV were identified, which can be attributed to the Bi-O bond [29,30]. These findings suggest that the $NaBH_4$ solution treatment was not fully effective in reducing BiOI to metal bismuth. In the O1s XPS high-resolution spectrum (Fig. S1b), peaks corresponding to Bi−*O* bonds (529.8 eV), hydroxyl groups (530.8 eV), and adsorbed water (532.6 eV) were observed [31]. Additionally, the peak at 532.6 eV may also be influenced by oxygen-containing functional groups (C—OH and C—O-C) present on the surface of the CC [7,32].

Based on the SEM images of the precursor (**Fig. S2a** and Fig. 1**d**), nanosheet arrays are uniformly distributed on the surface of CC. TEM image (**Fig. S2b**) further shows that the nanosheets in the arrays are composed of numerous small nanoparticles. HRTEM observations (Fig. 1**e**) reveal clear lattice fringes with a spacing of 0.328 nm, corresponding to the (012) crystal plane of metal Bi. Additionally, a significant amount of amorphous regions were observed, which can be attributed to the presence of amorphous bismuth oxide (BiO_x). The integrated results from HRTEM, XRD, and XPS confirm the coexistence of metal Bi and amorphous BiO_x in the precursor, leading us to designate it as CC/Bi-BiO_x. TGA (Fig. 1**f**) of the precursor provides valuable insights into the synthesis process of the final product. In both nitrogen and air atmospheres, the weight of the precursor remained relatively stable between 0 and 350 °C. This stability suggests a balance between the

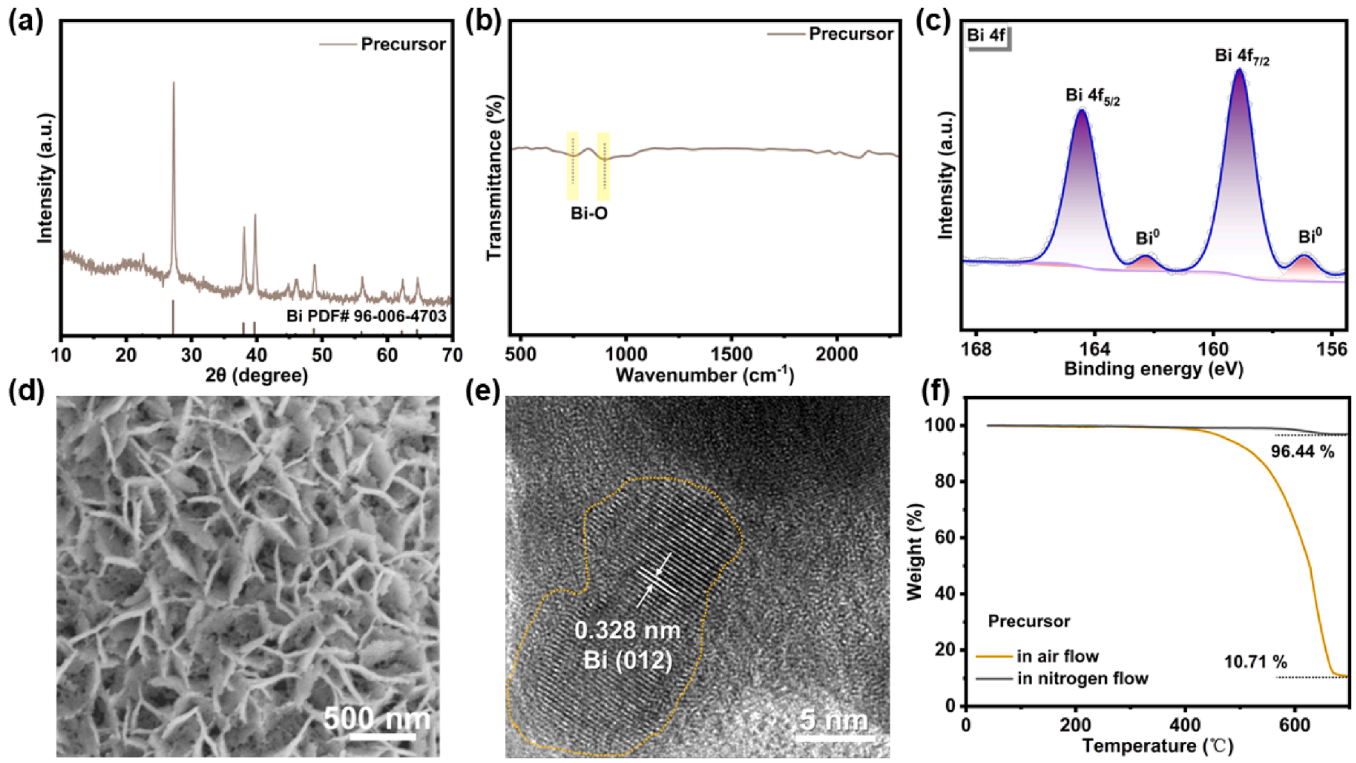

Fig. 1. a) XRD pattern. b) FTIR. c) high-resolution XPS spectrum of Bi 4f. d) SEM image. e) HRTEM image. f) TGA curves of the precursor.

weight gain due to Bi's oxidation and the weight loss from the pyrolysis of oxygen-containing functional groups on the CC [31]. In an air atmosphere, when the temperature exceeds 400 °C, the carbon fibers in CC/Bi-BiO_x begin to undergo pyrolysis and ultimately decompose completely. This suggests that the mass contribution of the CC accounts for approximately 90 % of the precursor. Under a nitrogen atmosphere,

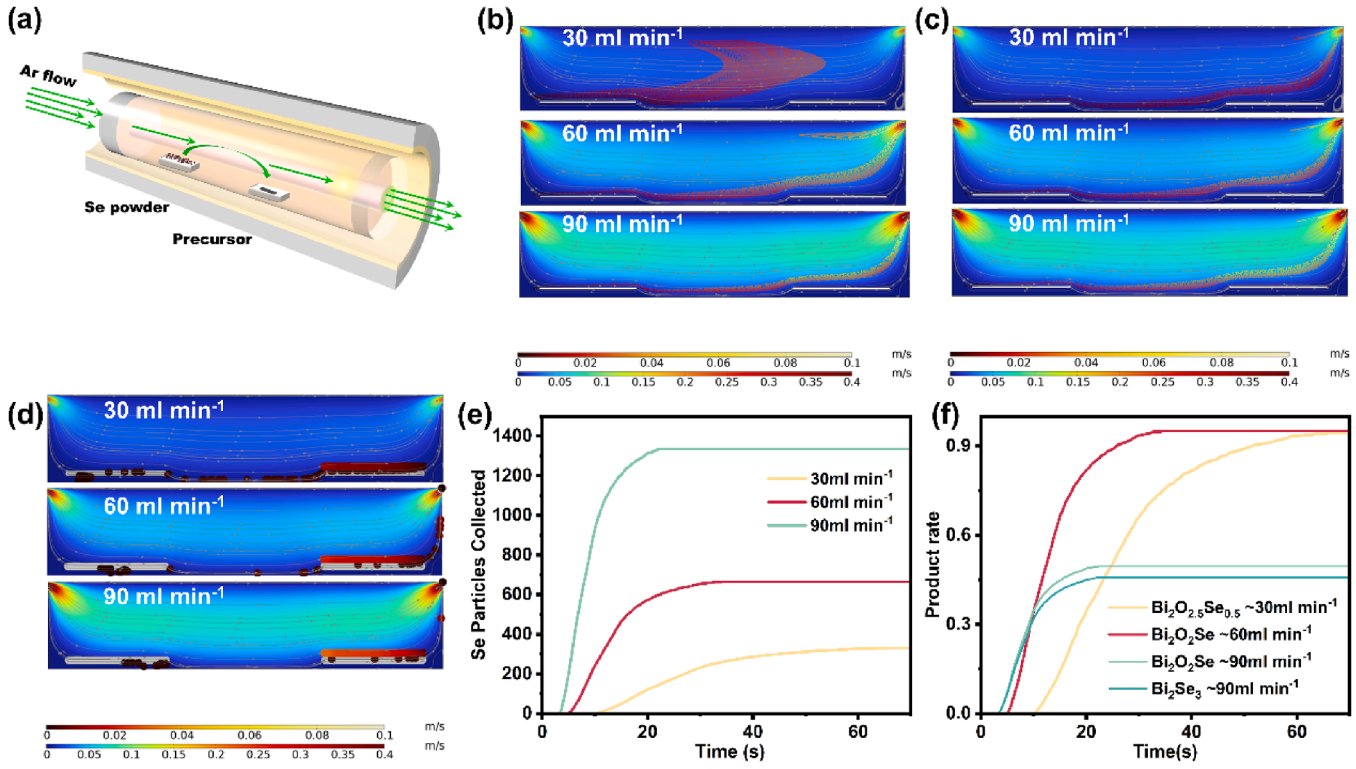

Fig. 2. a) Schematic diagram of preparation of different bismuth-based composite oxide electrodes by gas flow rate control. b) Se powder distribution in the reaction chamber (quartz tube) at the same time. c) spatial fluid and particle velocity distribution similar to the Se powder distribution near the surface. d) Se powder particle distribution under stable adhesion effect. e) the adsorption amount of Se powder particles by the precursor. f) the formation rate of different products at gas flow rate of 30 mL min^{-1}, 60 mL min^{-1}, 90 mL min^{-1}.

the CC/Bi-BiO_x sample exhibits a weight loss near 600 °C. This phenomenon is attributed to the catalytic effect of carbon in the protective atmosphere [33], which facilitates the reduction of bismuth oxide to form metal bismuth.

Through the CVD process conducted in a tube furnace (as depicted in the schematic diagram of Fig. 2**a**), different Se content products can be achieved by precisely controlling the gas flow rate. The quartz tube within the tube furnace serves as the reaction zone for CVD. Se powder is positioned upstream, while the CC/Bi-BiO_x precursor is placed downstream. By utilizing the COMSOL simulation method, we can perform a visual analysis of the Se introduction process and enhance our understanding of how different gas flow rates affect the doping level. Simulations (Fig. 2**b–d**) show that sublimated Se particles, transported by Ar gas, either adhere to the precursor surface due to single-particle adhesion effects, undergo chemical reactions, or are carried to the outlet by the gas flow.

Fig. 2**b** shows the distribution of Se powder particles over time under gas flow rates of 30, 60, and 90 mL min^{-1}. While transport behavior remains similar across different flow rates, shifting from wide-range transport to near-surface transport, higher flow rates (90 mL min^{-1}) accelerate near-surface adhesion and reaction onset. A stable vortex forms in the corner at lower speeds, but simulations indicate its limited influence on particle transport. Due to the small vortex radius (~0.25 cm) and the light weight of Se particles, unadhered particles are carried to the outlet by fast-moving gas. Fig. 2**c** reveals that Se powder exhibits similar spatial distribution before adhesion under all flow rates, with difference in particle number and velocity near the surface. Fig. 2**d** shows the stable adhesion state at different flow rates, where collected Se particles (dark circles) undergo adsorption and conversion into Se-containing Bi-based compounds. Particle color variations represent velocity differences before adsorption. By coupling the statistical information of adsorbed particles with the chemical reaction module, we obtained the synthesis conditions under three different gas flow rates, as shown in Fig. 2**e and f**). These results demonstrate that the adsorption amount of Se particles increases gradually with increasing gas flow rate. Moreover, the yields of the products corresponding to different flow rates are consistent with the experimentally obtained CC/$Bi_2O_{2.5}Se_{0.5}$, CC/Bi_2O_2Se, and CC/Bi_2O_2Se-Bi_2Se_3 compounds. The consistency between COMSOL simulation results and experimental data elucidates the microscopic mechanisms governing material transport and surface adsorption during the Se doping process controlled by gas flow rate. This deepens our understanding of the CVD strategy and provides a theoretical foundation for applying this method to the modification of various electrode materials in the future.

3.2. *Structure and morphology*

The phase characterization of the synthesized samples was performed using XRD, as illustrated in Fig. 3**a**. Analysis revealed that CC/Bi_2O_3 without Se source exhibited three prominent peaks at 27.9°, 31.7°, and 32.7°, corresponding to the (201), (002), and (220) planes of tetragonal β-Bi_2O_3 (PDF card No 97–041–7638). In contrast, the CC/$Bi_2O_{2.5}Se_{0.5}$ sample also displayed diffraction peaks, albeit with slightly diminished intensity compared to CC/Bi_2O_3. This observation suggests that CC/$Bi_2O_{2.5}Se_{0.5}$ retains the β-Bi_2O_3 phase structure. Based on the analysis of the local magnification diagram (**Fig. S3a**), the main diffraction peaks exhibit a slight shift towards lower angles. This shift is attributed to the increased lattice constant resulting from the incorporation of larger Se atoms. When the flow rate was 90 mL min^{-1}, the electrode exhibited distinct diffraction peaks at 24.0°, 29.2°, 31.8°, and 32.5°, indicating that with increasing Se content, the product no longer retained the β-Bi_2O_3 structure but instead formed tetragonal Bi_2O_2Se

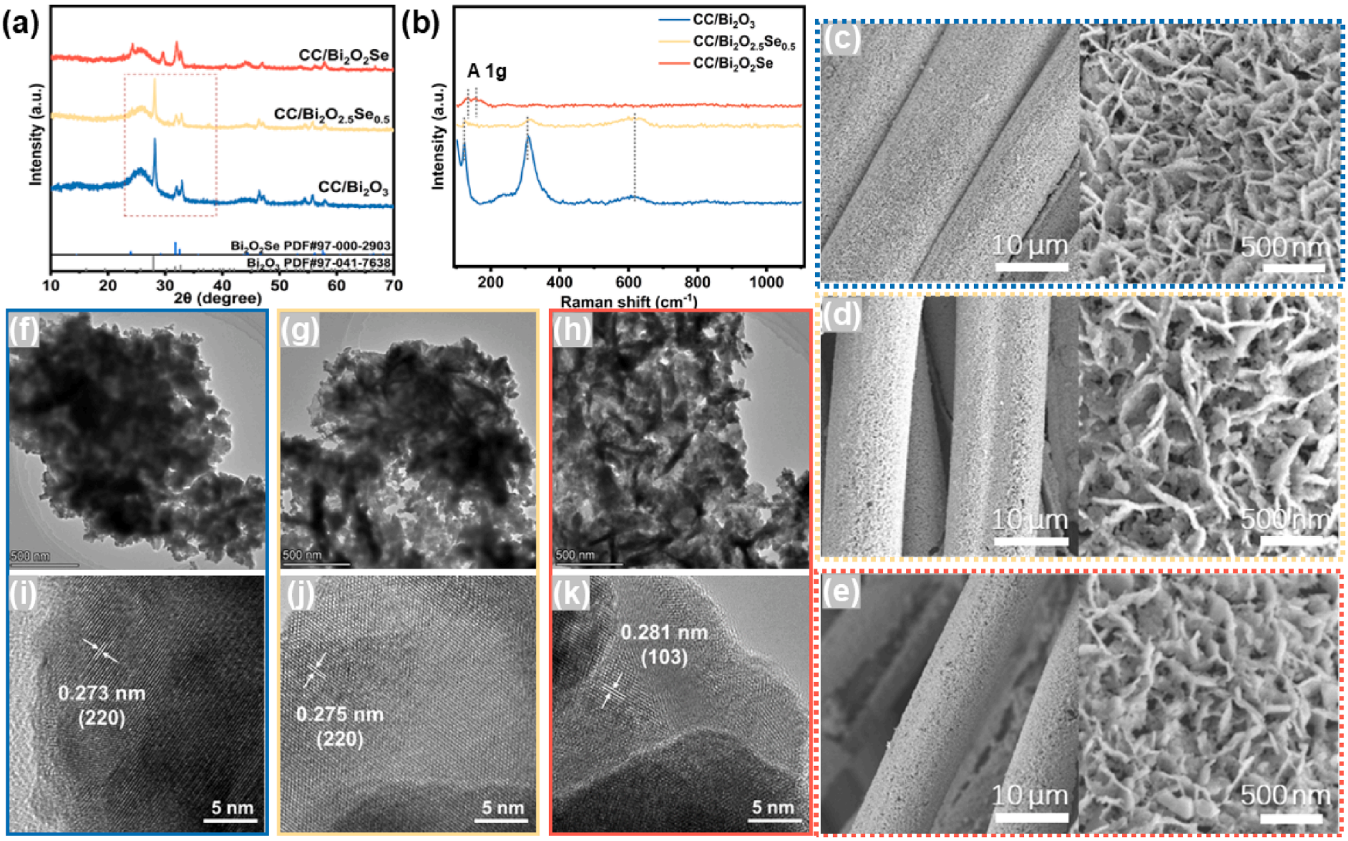

Fig. 3. a) XRD patterns. b) Raman spectra of CC/Bi_2O_3, CC/$Bi_2O_{2.5}Se_{0.5}$ and CC/Bi_2O_2Se. Low-magnification /high-magnification SEM images of c) CC/Bi_2O_3, d) CC/$Bi_2O_{2.5}Se_{0.5}$. e) CC/Bi_2O_2Se. TEM images of f) CC/Bi_2O_3. g) CC/$Bi_2O_{2.5}Se_{0.5}$ and (h) CC/Bi_2O_2Se. HRTEM images of i) CC/Bi_2O_3. j) CC/$Bi_2O_{2.5}Se_{0.5}$ and k) CC/Bi_2O_2Se.

(PDF card No 97–000–2930). Upon further increasing the flow rate, XRD results (**Fig. S3b**) revealed the formation of both Bi_2O_2Se-Bi_2Se_3 mixed phases and pure Bi_2Se_3 phase. The XRD analysis confirmed the effectiveness of the designed synthesis method in producing a series of samples with varying Se contents. Furthermore, subsequent electrochemical tests revealed that the CC/Bi_2O_2Se-Bi_2Se_3 and CC/Bi_2Se_3 samples exhibited relatively low electrochemical energy storage performance, which led to their exclusion from the primary focus of this study.

In the Raman spectroscopy results (Fig. 3**b**), peaks at approximately 125 cm^{-1} and 315 cm^{-1} were observed in both the CC/Bi_2O_3 and CC/$Bi_2O_{2.5}Se_{0.5}$ samples, corresponding to the stretching vibrations of Bi−*O* bonds in the β-Bi_2O_3 crystal structure [34,35]. Additionally, a broad peak was observed near 600 cm^{-1}, which is a distinctive feature unique to the β-phase Bi_2O_3 [36]. The CC/Bi_2O_2Se sample exhibits characteristic Raman peaks at approximately 133 cm^{-1} and 158 cm^{-1}, which can be attributed to the A1g vibration mode of Bi_2O_2Se [37]. The Raman and XRD results indicate that the CC/Bi_2O_3 sample prepared without a Se source exhibits the β phase of Bi_2O_3. After introducing a Se source, as the gas flow rate increases and the Se content in the product changes, the crystal structure evolves from Se-doped β-Bi_2O_3 (CC/$Bi_2O_{2.5}Se_{0.5}$) to the tetragonal Bi_2O_2Se structure (CC/Bi_2O_2Se).

The morphological characteristics of the prepared electrodes were examined using scanning electron microscopy (SEM). On the CC substrates, CC/Bi_2O_3, CC/$Bi_2O_{2.5}Se_{0.5}$, and CC/Bi_2O_2Se exhibited nearly identical vertical nanosheet array structures similar to those of their precursors. Notably, the thickness of the nanosheets progressively increased from CC/Bi_2O_3 to CC/Bi_2O_2Se, as illustrated in Fig. 3**c–e**. This nanosheet array structure significantly enhances the electrolyte contact area, thereby accelerating the kinetics of electrochemical reactions during energy storage [38,39]. In contrast, the edge thickness of the nanosheets in the CC/Bi_2O_2Se-Bi_2Se_3 and CC/Bi_2Se_3 samples increased significantly, while the pore structure within the nanosheets was nearly eliminated (see **Fig. S4**). The EDX analysis of all prepared electrode samples (**Fig. S5**) reveals that the Se element content on the surface of different samples exhibits a positive correlation with the gas flow rate during the preparation process. Through TEM images (Fig. 3**f–h**), it is confirmed that the nanosheets in the CC/Bi_2O_3, CC/$Bi_2O_{2.5}Se_{0.5}$, and

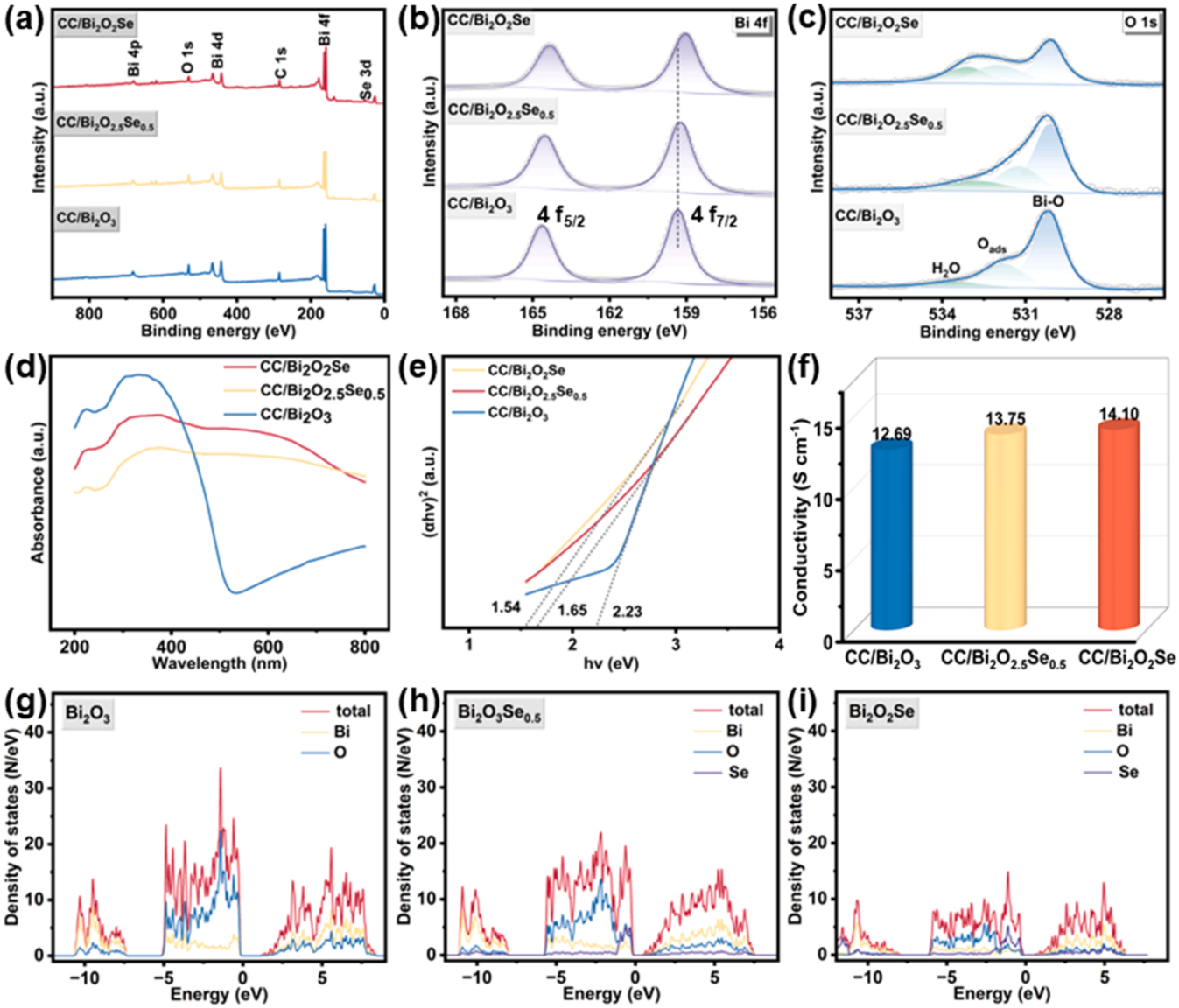

Fig. 4. a) XPS full spectrum. b) Bi 4f high resolution spectrum. c) O 1 s high resolution spectrum of CC/Bi_2O_3, CC/$Bi_2O_{2.5}Se_{0.5}$ and CC/Bi_2O_2Se. d) UV–vis spectra. e) Tauc diagrams. f) conductivity test results of CC/Bi_2O_3, CC/$Bi_2O_{2.5}Se_{0.5}$ and CC/Bi_2O_2Se. The total and projected density of states (DOS) curves of g) CC/Bi_2O_3, h) CC/$Bi_2O_{2.5}Se_{0.5}$ and i) CC/Bi_2O_2Se.

CC/Bi_2O_2Se samples are composed of numerous nanoparticles. In the HRTEM image of CC/Bi_2O_3 (Fig. 3**i**), lattice fringes with a spacing of 0.273 nm, corresponding to the (220) plane of β-Bi_2O_3, are clearly visible. Similarly, in the high-resolution transmission electron microscopy (HRTEM) image of the CC/$Bi_2O_{2.5}Se_{0.5}$ sample (Fig. 3**j**), lattice fringes corresponding to the (220) plane of β-Bi_2O_3 are also observed. However, the interplanar spacing increased slightly to 0.275 nm, indicating that Se doping into β-Bi_2O_3 results in larger unit cell parameters in $Bi_2O_{2.5}Se_{0.5}$ compared to the original β-Bi_2O_3 due to the larger atomic radius of Se. This observation is consistent with the previous XRD results. In the HRTEM image of CC/Bi_2O_2Se (Fig. 3**k**), lattice fringes with a spacing of 0.281 nm can be observed, corresponding to the (103) plane of tetragonal Bi_2O_2Se.

The chemical states and binding energies of CC/Bi_2O_3, CC/$Bi_2O_{2.5}Se_{0.5}$, and CC/Bi_2O_2Se were analyzed using XPS. According to the full-spectrum XPS scans (Fig. 4**a**), the CC/Bi_2O_3 sample exhibited characteristic peaks for Bi, C, and O elements, whereas the CC/$Bi_2O_{2.5}Se_{0.5}$ and CC/Bi_2O_2Se samples showed additional characteristic peaks corresponding to Se, in addition to Bi, C, and O. In the high-resolution Bi 4f spectrum (Fig. 4**b**), two peaks are observed at binding energies of 159.3 eV and 164.6 eV, corresponding to the $4f_{7/2}$ and $4f_{5/2}$ orbitals of Bi^{3+} in the Bi−*O* bond [40]. Compared to CC/Bi_2O_3, the Bi $4f_{7/2}$ and $4f_{5/2}$ orbitals of CC/$Bi_2O_{2.5}Se_{0.5}$ and CC/Bi_2O_2Se exhibit a negative shift, which can be attributed to the presence of Bi−Se bonds, as the binding energy of Bi−Se is lower than that of Bi−*O* [41]. Due to the lower electronegativity of Se, its introduction results in altered bond lengths and changes in the metal coordination environment within metal oxides, leading to the observed shifts in binding energy in XPS [15,42,43]. In the high-resolution XPS spectra of O1s, peaks at 530.1, 531.7, and 533.5 eV are observed, corresponding to lattice oxygen (Bi−*O*), adsorbed oxygen, and oxygen in H_2O [44], respectively (Fig. 4**c**). In the series of samples from CC/Bi_2O_3 to CC/Bi_2O_2Se, the intensity of the Bi−*O* peak gradually decreases, which is consistent with the progressive reduction in oxygen content within their crystal structures. In the XPS spectra of CC/$Bi_2O_{2.5}Se_{0.5}$ and CC/Bi_2O_2Se, the peaks at 53.5 and 54.6 eV (**Fig. S6**) are attributed to the Se^{2-} $3d_{5/2}$ and Se^{2-} $3d_{3/2}$ signals, respectively [45]. The peak near 56 eV is assigned to the oxidized state's SeO_x [46].

Based on the UV–vis results (Fig. 4**d**), the Tauc method can be employed to estimate the band gaps (Eg) of CC/Bi_2O_3, CC/$Bi_2O_{2.5}Se_{0.5}$, and CC/Bi_2O_2Se. The Eg of CC/Bi_2O_3, CC/$Bi_2O_{2.5}Se_{0.5}$, and CC/Bi_2O_2Se are 2.23 eV, 1.65 eV, and 1.54 eV (Fig. 4**e**), respectively. The observed narrowing of the band gap upon Se incorporation suggests that introducing Se into bismuth-based oxides facilitates electron excitation from the valence band to the conduction band, thereby enhancing the material's electrical conductivity. The results of the four-probe method test (Fig. 4**f**) indicate that the electrical conductivity of CC/$Bi_2O_{2.5}Se_{0.5}$ and CC/Bi_2O_2Se is significantly higher than that of CC/Bi_2O_3, consistent with the trend observed in the band gap measurements. This suggests that introducing Se into the bismuth oxide system effectively enhances electron migration within the material structure. Through density of states (DOS) calculations for bulk materials, we determined that the band gaps of Bi_2O_3, $Bi_2O_{2.5}Se_{0.5}$, and Bi_2O_2Se are 1.43 eV, 0.76 eV, and 0.51 eV, respectively (Fig. 4***g–i***). The top of the valence band is primarily composed of contributions from the O element. Upon doping Se into the ideal tetragonal phase of Bi_2O_3, the density of states (DOS) associated with Se becomes more pronounced near the Fermi level and within the conduction band region. This indicates that Se doping introduces new energy levels and potentially enhances the probability of electron transitions, thereby reducing the material's band gap. In comparison with the layered structure of Bi_2O_2Se, as the Se content increases, the top of the valence band is increasingly dominated by Se contributions, leading to a further reduction in the band gap. This facilitates enhanced electron transfer and conductivity.

3.3. Electrochemical performance

The electrochemical performance of the prepared electrodes was evaluated in 1 M $ZnSO_4$ electrolyte. CV curves at a scan rate of 3 mV s^{-1} revealed distinct redox peaks for all samples, with CC/$Bi_2O_{2.5}Se_{0.5}$ and CC/Bi_2O_2Se showing significantly enhanced peak currents, indicating superior electrochemical activity (Fig. 5**a**). Notably, the resolved anodic/cathodic peaks do not strictly appear as one-to-one pairs. This arises from partly irreversible conversion in CC/Bi_2O_3 (suppressing the return peak), multi-step conversion with overlapping features in CC/$Bi_2O_{2.5}Se_{0.5}$, and pronounced pseudocapacitive H^+-intercalation in CC/Bi_2O_2Se that broadens or masks discrete couples at the chosen scan rate (see Fig. 6**a–c**), which is consistent with operando/ex-situ observations of dual intercalation–conversion mechanisms and strong capacitive contributions in Bi_2O_2Se, and with H^+/Zn^{2+} co-insertion leading to activation-dependent merging/splitting of peaks in BiOSe [47,48]. GCD profiles at 0.5 A g^{-1} demonstrated longer discharge times and higher specific capacities for CC/$Bi_2O_{2.5}Se_{0.5}$ and CC/Bi_2O_2Se compared to other samples, with CC/Bi_2O_2Se achieving a maximum specific capacity of 312.5 mAh g^{-1} at 0.1 A g^{-1} (Fig. 5**b**). This performance is comparable to the upper-limit conversion capacity of Bi_2O_2Se (304.0 mAh g^{-1}; $n = 6$, $Q_{th} = nF/3.6$ M) and is significantly higher than that of pristine Bi_2O_3 (see Supplementary Table S1). The slight apparent excess (~2.8 %) likely arises from minor pseudocapacitive/double-layer contributions and uncertainty in active-mass determination by differential weighing, rather than conversion beyond the theoretical limit. Furthermore, the CC/$Bi_2O_{2.5}Se_{0.5}$ and CC/Bi_2O_2Se samples demonstrate significantly longer discharge times and higher specific capacities compared to other samples. By examining the specific capacity values of each electrode at various current densities (see Fig. 5**c**), it is evident that the capacity of CC/Bi_2O_3 is 101.6 mAh g^{-1} at a current density of 0.1 A g^{-1}, but sharply decreases to 4 mAh g^{-1} at 2 A g^{-1}. At various current densities, the capacity of CC/Bi_2O_3 rapidly decreased from 101.6 mAh g^{-1} at 0.1 A g^{-1} to 4 mAh g^{-1} at 2 A g^{-1}, while CC/ $Bi_2O_{2.5}Se_{0.5}$ and CC/Bi_2O_2Se maintained much higher capacities (Fig. 5**c**). Compared with other bismuth-based electrode materials used for zinc-ion energy storage [12,49–52], CC/$Bi_2O_{2.5}Se_{0.5}$ and CC/Bi_2O_2Se exhibited significant specific capacity advantages (Fig. 5**d**). Notably, CC/Bi_2O_2Se achieves a maximum specific capacity of 312.5 mAh g^{-1} at a current density of 0.1 A g^{-1}, approaching the theoretical specific capacity of bismuth oxides. To exclude any contribution from the substrate, we prepared annealed carbon cloth and Se-annealed carbon cloth under identical thermal conditions but without the Bi precursor; both controls exhibit only CC peaks in XRD, negligible mass change, and capacities below 10 mAh g^{-1} (Figs. S7–S8).

The power density and energy density of the CC/Bi_2O_2Se||Zn cell (Fig. 5**e**) exhibit notable advantages compared to other zinc-ion batteries [11,12,52–58]. In continuous rate charge-discharge tests, CC/Bi_2O_3's capacity decayed rapidly within a few cycles at 0.2 A g^{-1}, while CC/$Bi_2O_{2.5}Se_{0.5}$ and CC/Bi_2O_2Se stabilized after high-current cycles and switching to low-current conditions (Fig. 5**f**). Long-term cycling stability tests at 2 A g^{-1} showed that CC/Bi_2O_3's capacity decayed quickly within the initial cycles, whereas CC/$Bi_2O_{2.5}Se_{0.5}$ and CC/Bi_2O_2Se maintained retention rates above 60 % after 4000 cycles, with CC/Bi_2O_2Se achieving a superior retention rate of 74.6 % (Fig. 5***g***). This indicates that selenium incorporation significantly enhances the capacity retention of the electrode material. The mechanism underlying the rapid capacity fade of Bi_2O_3 in $ZnSO_4$ electrolyte and the effective mitigation by Se will be discussed in detail in the next section.

To evaluate the adaptability of introducing Se into bismuth oxides across different electrochemical systems, we investigated the electrochemical energy storage performance of CC/Bi_2O_2Se and CC/Bi_2O_3 electrodes in alkaline electrolytes (**Fig. S9**). The maximum specific capacitance of CC/Bi_2O_2Se reached 644 F g^{-1} at 1 A g^{-1}, approximately twice that of CC/Bi_2O_3. The alkaline aqueous battery device assembled with CC/Bi_2O_2Se as the anode and nickel hydroxide fluoride as the

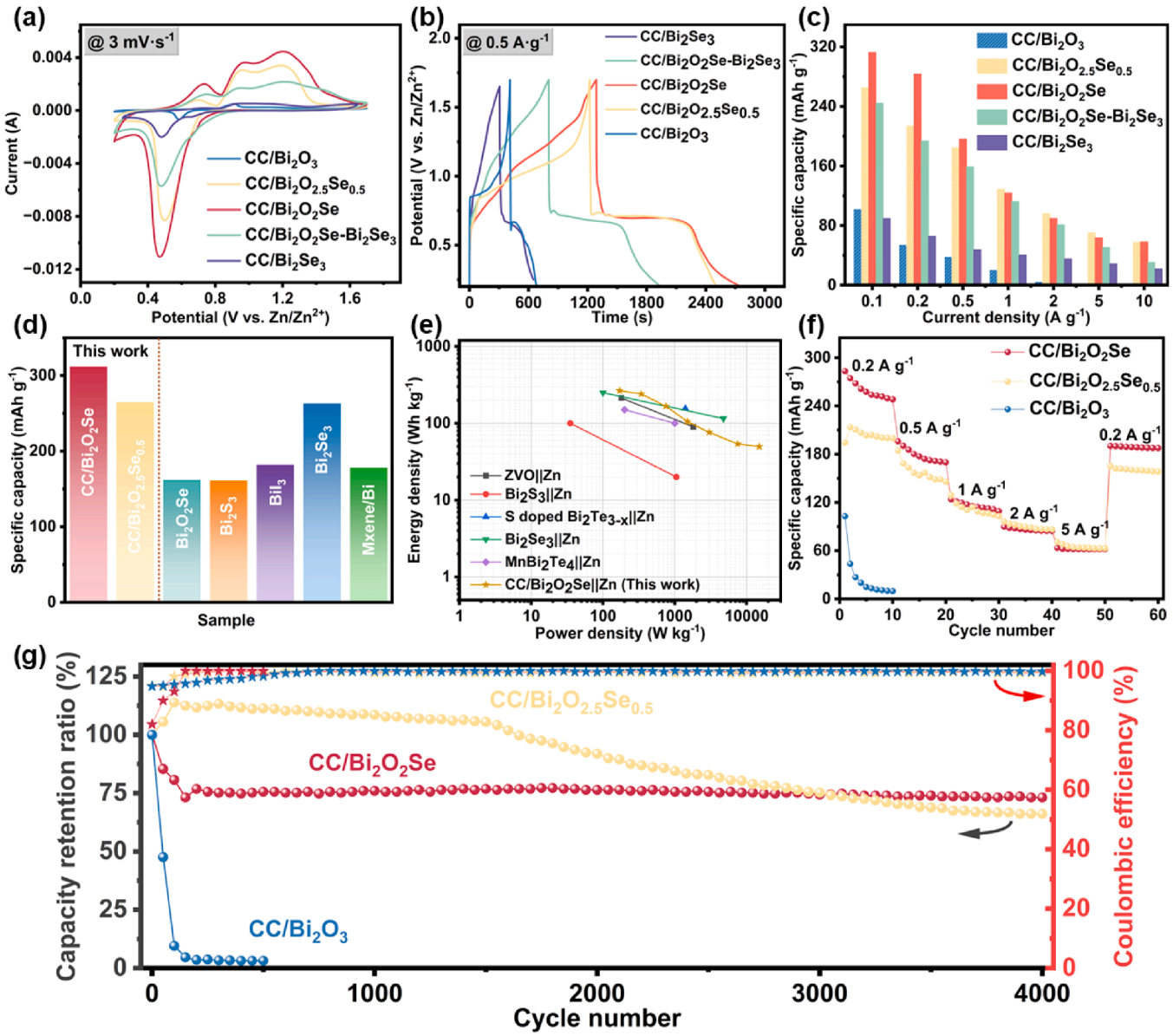

Fig. 5. a) CV curves at 3 mV s^{-1}. b) GCD profiles at 0.5 A g^{-1}. c) specific capacity values at different current densities of CC/Bi_2O_3, CC/$Bi_2O_{2.5}Se_{0.5}$, CC/Bi_2O_2Se, CC/Bi_2O_2Se-Bi_2Se_3 and CC/Bi_2Se_3. d) Comparison of the maximum capacity of CC/$Bi_2O_{2.5}Se_{0.5}$ and CC/Bi_2O_2Se with other Bi-based electrode materials. e) Ragone plots of CC/Bi_2O_2Se||Zn. f) Continuous charge and discharge tests of CC/Bi_2O_3, CC/$Bi_2O_{2.5}Se_{0.5}$ and CC/Bi_2O_2Se at different rates. g) Cycle stability tests of CC/Bi_2O_3, CC/$Bi_2O_{2.5}Se_{0.5}$ and CC/Bi_2O_2Se.

cathode achieved a maximum energy density of 83.3 Wh kg^{-1} and a maximum power density of 30,000 W kg^{-1}. This result further confirms the effectiveness of introducing Se to modulate the electronic structure of bismuth oxide.

3.4. Mechanism of electrochemical reactions

By analyzing the voltage differences of the charge/discharge platforms for CC/Bi_2O_3, CC/$Bi_2O_{2.5}Se_{0.5}$, and CC/Bi_2O_2Se at various current densities (**Fig. S10**), it was observed that the voltage difference of CC/Bi_2O_3 increased more significantly with increasing current density compared to CC/$Bi_2O_{2.5}Se_{0.5}$ and CC/Bi_2O_2Se. This suggests that CC/Bi_2O_3 exhibits a higher degree of polarization, characterized by slower redox reaction kinetics and poorer reversibility [59].

Based on the cyclic voltammetry curves at various scan rates (**Fig. S11**), the b values for the oxidation and reduction processes of the three electrodes were calculated (Fig. 6**a–c**). CC/Bi_2O_3 exhibited significant differences in b values between its oxidation and reduction processes, likely due to its irreversible reaction characteristics. In contrast, CC/$Bi_2O_{2.5}Se_{0.5}$ had a b value of 0.61 for the reduction process, while CC/Bi_2O_2Se had a higher b value of 0.83, indicating that the reduction process of CC/$Bi_2O_{2.5}Se_{0.5}$ is more diffusion-limited. This suggests distinct electrochemical energy storage mechanisms between CC/$Bi_2O_{2.5}Se_{0.5}$ and CC/Bi_2O_2Se. Additionally, using the Dunn method k1 value (**Fig. S12**), the capacitance contribution of CC/Bi_2O_2Se was found to be consistently higher across all scan rates compared to CC/Bi_2O_3 and $Bi_2O_{2.5}Se_{0.5}$, indicating less diffusion limitation and greater involvement of pseudocapacitive processes, such as surface redox reactions or intercalation pseudocapacitance.

In-situ electrochemical impedance spectroscopy measurements were performed on the discharge and charge processes of the three electrodes to construct three-dimensional Bode plots, illustrating the phase angle (φ) - frequency (*f*) relationship at various potentials (Fig. 6**d-i**). These plots enable real-time monitoring of electrode reaction kinetics during

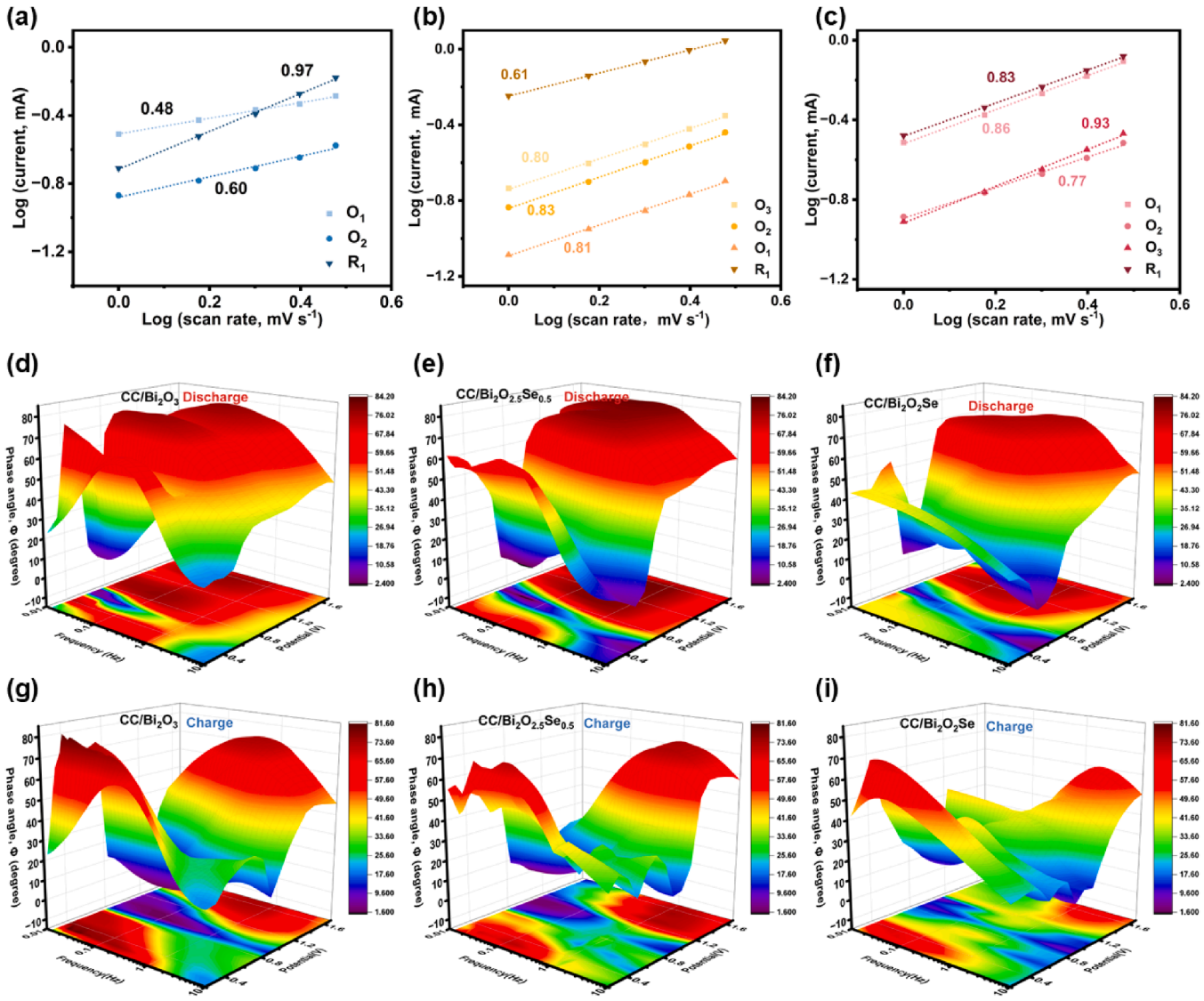

Fig. 6. Power law exponentials (b values) of a) CC/Bi_2O_3, b) $CC/Bi_2O_{2.5}Se_{0.5}$ and c) CC/Bi_2O_2Se. 3D Bode-phase plots during discharge of d) CC/Bi_2O_3, e) $CC/Bi_2O_{2.5}Se_{0.5}$ and f) CC/Bi_2O_2Se. 3D Bode-phase plots during charge of g) CC/Bi_2O_3, h) $CC/Bi_2O_{2.5}Se_{0.5}$ and i) CC/Bi_2O_2Se.

electrochemical processes [60]. The region where the phase angle φ is closer to 90° indicates a behavior more akin to capacitance, while the area where φ is closer to 0° suggests that the behavior at that potential is more diffusion-controlled, with a phase change (ion intercalation/deintercalation or conversion reaction) occurring at the electrode [61]. In the three-dimensional Bode plots of the CC/Bi_2O_3, $CC/Bi_2O_{2.5}Se_{0.5}$, and CC/Bi_2O_2Se electrodes shown in Fig. 6**d–i**, regions with very low phase angles φ (depicted as dark blue and purple) are observed. These regions generally correspond to the plateaus during the charge and discharge processes, indicating that phase transitions occur during their electrochemical reactions. The significant differences observed in the low phase angle regions during the discharge (Fig. 6**d**) and charge (Fig. 6**g**) processes of the CC/Bi_2O_3 electrode are attributed to its poor electrochemical reversibility. The smaller low-phase-angle regions observed in the CC/Bi_2O_2Se electrode (Fig. 6**f–i**) suggest faster electrochemical reaction kinetics, which may be attributed to the previously reported H^+ intercalation/deintercalation-dominated mechanism of Bi_2O_2Se. The smaller ionic radius of H^+ facilitates rapid diffusion [50]. These kinetic features rationalize the asymmetric number of anodic/cathodic peaks in CV: CC/Bi_2O_3 shows mismatched b-values consistent with partial irreversibility, $CC/Bi_2O_{2.5}Se_{0.5}$ exhibits diffusion-limited multi-step conversion that merges into composite peaks, and CC/Bi_2O_2Se displays higher capacitive contributions (k_1 fraction) and smaller low-phase-angle regions in the 3D Bode plots, which broaden or obscure discrete redox couples (Fig. 6a-i).

To investigate the significant differences in specific capacity and cycling stability between the CC/Bi_2O_3, $CC/Bi_2O_{2.5}Se_{0.5}$ and CC/Bi_2O_2Se samples, we focus on the emergence and reversibility of metallic Bi and analyzed the variations in electrochemical reactions during charging and discharging by comparing their XRD patterns at different potentials (Fig. 7**a–c**). In the XRD patterns of the CC/Bi_2O_3 sample at different potentials (Fig. 7**a**), it is clearly observed that Bi_2O_3 undergoes transformation into metallic Bi and cannot revert to its initial crystalline β-Bi_2O_3 state. A minor diffraction peak at approximately 33.2° is observed, which can be attributed to the formation of basic zinc sulfate hexahydrate ($Zn_4(OH)_6SO_4{\cdot}4H_2O$, ZHS, JCPDS card No 44–0673), likely resulting from a side reaction. This indicates that the electrochemical reaction involves the irreversible conversion of Bi_2O_3 to metallic Bi, leading to poor cycling stability. In contrast, during the charge and discharge process of $CC/Bi_2O_{2.5}Se_{0.5}$, its phase corresponds to metallic Bi in the discharged state (as shown in V. in Fig. 7**b**), and to $Bi_2O_{2.7}$ in the charged state (as shown in III. in Fig. 7**b**), indicating that a reversible transformation reaction occurs during its electrochemical process, involving the conversion between Bi^0 and Bi^{3+}. The phase of

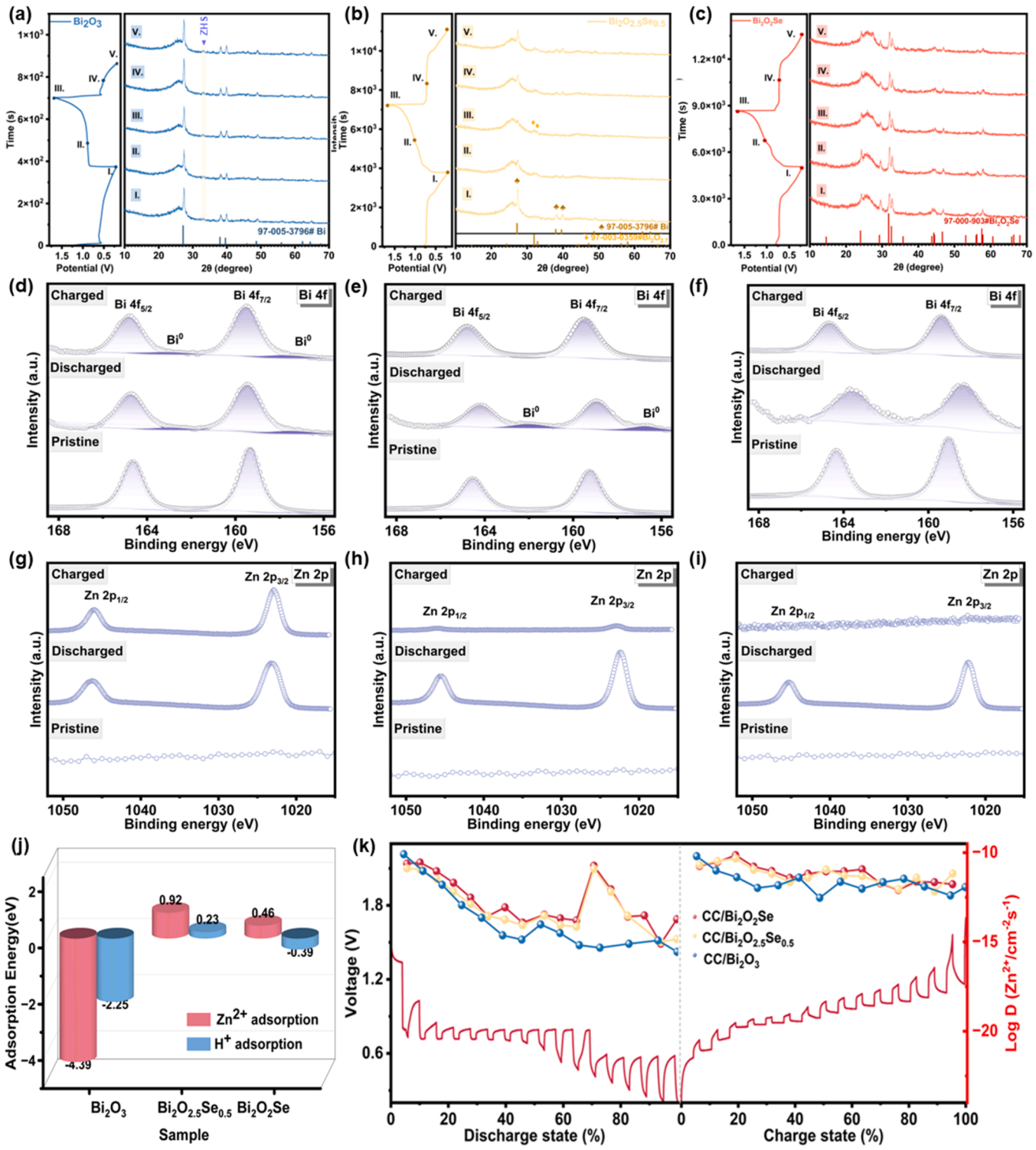

Fig. 7. XRD patterns of a) CC/Bi_2O_3, b) CC/$Bi_2O_{2.5}Se_{0.5}$ and c) CC/Bi_2O_2Se at different potentials during charge and discharge. Bi 4f high-resolution XPS spectra of d) CC/Bi_2O_3, e) CC/$Bi_2O_{2.5}Se_{0.5}$ and f) CC/Bi_2O_2Se at three states of original/fully discharged/fully charged. Zn 2p high-resolution XPS spectra of g) CC/Bi_2O_3, h) CC/$Bi_2O_{2.5}Se_{0.5}$ and i) CC/Bi_2O_2Se at three states of original/fully discharged/fully charged. j) Adsorption energy of Bi_2O_3, $Bi_2O_{2.5}Se_{0.5}$ and Bi_2O_2Se. k) GITT curve of CC/Bi_2O_2Se and diffusion coefficient of CC/Bi_2O_3, CC/$Bi_2O_{2.5}Se_{0.5}$, CC/Bi_2O_2Se.

CC/Bi_2O_2Se with a layered structure remains Bi_2O_2Se at different charge and discharge potentials (Fig. 7**c**), and no obvious positional shift is observed whether in the fully charged or fully discharged state. This can be attributed to the small radius of H^+ ions, which causes insignificant structural strain during the insertion and extraction process in the Bi_2O_2Se material [50]. Compared with CC/Bi_2O_3 which undergoes a lowly reversible conversion reaction, CC/$Bi_2O_{2.5}Se_{0.5}$ exhibits a more highly reversible conversion reaction mechanism, while CC/Bi_2O_2Se features a H^+ intercalation-deintercalation reaction mechanism that causes less structural damage. Therefore, the cycling stability of these two materials is significantly better than that of CC/Bi_2O_3.

Compared with CC/$Bi_2O_{2.5}Se_{0.5}$ and CC/Bi_2O_2Se, the binding energy

shift in the high-resolution Bi 4f XPS spectra of CC/Bi_2O_3 (Fig. 7**d**) is minimal in both fully discharged and charged states, indicating a limited number of active Bi species available for electrochemical reactions. This observation is further supported by the Zn 2p spectra of CC/Bi_2O_3 (Fig. 7***g***), which reveal the presence of significant amounts of Zn species on the Bi_2O_3 surface in both states, consistent with the formation of ZHS. The SEM and EDX analysis of the surface (**Fig. S13**) also corroborates this finding. In contrast, the ZHS in the CC/$Bi_2O_{2.5}Se_{0.5}$ and CC/Bi_2O_2Se samples exhibits reversible deposition and dissolution during the charge-discharge process (Fig. 7**h–i**).

The results of the adsorption energy calculations (Fig. 7**j and Fig. S14**) reveal that Bi_2O_3 exhibits an extremely strong adsorption capacity for Zn^{2+} (−4.39 eV), enabling stable adsorption of Zn^{2+} on its surface and leading to excessive enrichment. In contrast, $Bi_2O_{2.5}Se_{0.5}$ and Bi_2O_2Se show relatively weak adsorption capacities for Zn^{2+}, preventing stable adsorption and thereby avoiding irreversible deposition of ZHS byproducts upon Zn^{2+} reduction, which is crucial for maintaining the electrode's good reversibility. The differences in H^+ adsorption energies between Bi_2O_2Se and $Bi_2O_{2.5}Se_{0.5}$ may also contribute to the distinct reaction mechanisms observed in their XRD patterns during charge-discharge processes. Additionally, the diffusion coefficients of the three electrodes, measured using galvanostatic intermittent titration technique (GITT) (Fig. 7**k**), followed the order: CC/Bi_2O_2Se > CC/$Bi_2O_{2.5}Se_{0.5}$ > CC/Bi_2O_3. The highest diffusion coefficient for CC/Bi_2O_2Se is attributed to its layered structure and efficient H^+ intercalation-deintercalation mechanism, facilitated by the small size of H^+. Conversely, CC/Bi_2O_3 exhibited the lowest diffusion coefficient due to its strong interaction with Zn^{2+}, which causes irreversible ZHS deposition and hinders ion migration and diffusion. During charge-discharge cycles, the electrolyte near the CC/$Bi_2O_{2.5}Se_{0.5}$ electrode shows a more pronounced change in conductivity compared to that near the CC/Bi_2O_3 electrode (**Fig. S15**), indicating a higher concentration of active bismuth species participating in electrochemical reactions and greater consumption of ionic charge carriers in the electrolyte.

To further investigate the role of ZHS formation in the electrochemical performance, we tested the electrodes in a 1 M $ZnSO_4$-EG electrolyte. The results showed that CC/Bi_2O_3 exhibited improved reversibility in EG-based electrolyte compared to aqueous solutions, likely due to the suppression of ZHS formation (**Fig. S16**) [13,56]. This observation underscores the importance of by-product formation in the capacity fade of Bi_2O_3 and suggests that designing suitable electrolytes could be a promising strategy for enhancing Zn^{2+} storage efficiency in bismuth oxides. To further quantify the relative roles of Zn^{2+} and H^+, we performed a semi-quantitative partition using the $ZnSO_4$–EG control. Based on capacities at 0.1 A g^{-1} in aqueous $ZnSO_4$ and $ZnSO_4$–EG (Fig. 5 **and Fig. S16**), the estimated Zn^{2+}/H^+ fractions are ~75/25 for CC/ CC/Bi_2O_3, ~45/55 for CC/$Bi_2O_{2.5}Se_{0.5}$, and ~29/71 for CC/ Bi_2O_2Se (details in **Table S2**).

4. Conclusions

In this study, we successfully demonstrated that selenium incorporation into bismuth oxide significantly enhances the electrochemical performance for zinc-ion storage. By controlling the gas flow rate during chemical vapor deposition, we synthesized a series of bismuth-based compounds with varying Se contents. Notably, CC/$Bi_2O_{2.5}Se_{0.5}$ and CC/Bi_2O_2Se exhibited substantial improvements in specific capacity and cycling stability compared to pristine Bi_2O_3. CC/Bi_2O_2Se achieved a maximum specific capacity of 312.5 mAh g^{-1} at 0.1 A g^{-1}, with a retention rate of 74.6 % after 4000 cycles at 2 A g^{-1}. These enhancements are attributed to the narrowed band gap and improved electrical conductivity from Se doping, which facilitates electron and ion transport. Additionally, Se incorporation stabilizes the $Bi^{3+}\leftrightarrow Bi^{\circ}$ conversion and mitigates the formation of detrimental by-products, ensuring more reversible and efficient Zn-ion storage. Our findings highlight the importance of electronic structure regulation in optimizing metal oxide electrodes and provide valuable insights for designing high-performance energy storage materials. Future work will explore other dopants and optimize synthesis conditions to further enhance electrochemical properties for practical applications.

CRediT authorship contribution statement

Jian Xu: Writing – original draft, Investigation, Data curation. **Jingchen Zhang:** Software, Formal analysis. **Zeyu Hao:** Writing – review & editing, Visualization, Validation. **Xiliang Gong:** Methodology, Conceptualization. **Zeshuo Meng:** Methodology, Conceptualization. **Yutong Zhao:** Writing – review & editing. **Shulong Wang:** Visualization. **Haoteng Sun:** Software, Formal analysis. **Hongwei Tian:** Writing – review & editing, Supervision, Resources, Project administration, Funding acquisition. **Dawei Su:** Resources.

Declaration of competing interest

The authors declare that they have no known competing financial interests or personal relationships that could have appeared to influence the work reported in this paper.

Acknowledgements

J. Xu, J. Zhang and Z. Hao contributed equally to this work. This work was financially supported by the Scientific and Technological Development Program of Jilin Province (grant no 20240101114JC).

Supplementary materials

Supplementary material associated with this article can be found, in the online version, at doi:10.1016/j.actamat.2025.121701.

References

[1] H. Li, L. Ma, C. Han, Z. Wang, Z. Liu, Z. Tang, C. Zhi, Advanced rechargeable zinc-based batteries: recent progress and future perspectives, Nano Energy 62 (2019) 550–587, https://doi.org/10.1016/j.nanoen.2019.05.059.
[2] W. Lv, J. Liu, Z. Shen, X. Li, C. Xu, Novel approaches to aqueous zinc-ion batteries: challenges, strategies, and prospects, eScience (2025) 100410, https://doi.org/10.1016/j.esci.2025.100410.
[3] J. Hao, X. Li, X. Zeng, D. Li, J. Mao, Z. Guo, Deeply understanding the Zn anode behaviour and corresponding improvement strategies in different aqueous Zn-based batteries, Energy Environ. Sci. 13 (2020) 3917–3949, https://doi.org/10.1039/D0EE02162H.
[4] Z. Tie, Y. Zhang, J. Zhu, S. Bi, Z. Niu, An air-rechargeable Zn/organic battery with proton storage, J. Am. Chem. Soc. 144 (2022) 10301–10308, https://doi.org/10.1021/jacs.2c01485.
[5] J. Ni, X. Bi, Y. Jiang, L. Li, J. Lu, Bismuth chalcogenide compounds Bi2×3 (X=O, S, Se): applications in electrochemical energy storage, Nano Energy 34 (2017) 356–366, https://doi.org/10.1016/j.nanoen.2017.02.041.
[6] G. Zan, T. Wu, P. Hu, Y. Zhou, S. Zhao, S. Xu, J. Chen, Y. Cui, Q. Wu, An approaching-theoretical-capacity anode material for aqueous battery: hollow hexagonal prism Bi2O3 assembled by nanoparticles, Energy Storage Mater. 28 (2020) 82–90, https://doi.org/10.1016/j.ensm.2020.02.027.
[7] J. Wang, Y. Huang, S. Zhang, X. Du, Z. Duan, X. Sun, Hollow Co9S8 cores encapsulated in hierarchical MXene@Bi2O3 multiple shells for constructing binder-free electrodes of foldable supercapacitors, J. Mater. Sci. Technol. 147 (2023) 112–123, https://doi.org/10.1016/j.jmst.2022.10.071.
[8] W. Wang, Y. Xiao, X. Li, Q. Cheng, G. Wang, Bismuth oxide self-standing anodes with concomitant carbon dots welded graphene layer for enhanced performance supercapacitor-battery hybrid devices, Chem. Eng. J. 371 (2019) 327–336, https://doi.org/10.1016/j.cej.2019.04.048.
[9] D. Wang, Y. Zhao, G. Liang, F. Mo, H. Li, Z. Huang, X. Li, T. Tang, B. Dong, C. Zhi, A zinc battery with ultra-flat discharge plateau through phase transition mechanism, Nano Energy 71 (2020) 104583, https://doi.org/10.1016/j.nanoen.2020.104583.
[10] Y. Zong, H. Chen, J. Wang, M. Wu, Y. Chen, L. Wang, X. Huang, H. He, X. Ning, Z. Bai, W. Wen, D. Zhu, X. Ren, N. Wang, S. Dou, Cation defect-engineered boost fast kinetics of two-dimensional topological Bi2Se3 cathode for high-performance aqueous Zn-ion batteries, Adv. Mater. 35 (2023) 2306269, https://doi.org/10.1002/adma.202306269.
[11] L. Chen, X. Liang, X. Wang, G. Peng, H. Xie, Modifying electronic structure of bismuth telluride through S doping and Te vacancy engineering for enhanced Zn-

ion storage ability in aqueous Zn-proton hybrid ion batteries, Small. 20 (2024) 2306697, https://doi.org/10.1002/smll.202306697.
[12] T. Xiong, Y. Wang, B. Yin, W. Shi, W.S.V. Lee, J. Xue, Bi2S3 for aqueous Zn ion battery with enhanced cycle stability, Nanomicro Lett. 12 (2019) 8, https://doi.org/10.1007/s40820-019-0352-3.
[13] K. Guo, Y. Li, C. Yang, Y. Xiang, S. Pan, Q. Zeng, Z. Li, N. Yu, X. Wang, Metallic vanadium activated by an in situ dissolution–deposition process for a superior aqueous zinc ion battery cathode, Chem. Commun. 61 (2025) 2329–2332, https://doi.org/10.1039/D4CC06362G.
[14] Q. Zeng, S. Zhou, N. Yu, J. Huo, C. Sun, K. Guo, In situ electrochemical activation enabling high-performance cathodes for aqueous zinc-ion batteries, J. Mater. Chem. A 13 (2025) 24997–25007, https://doi.org/10.1039/D5TA03493K.
[15] W. Song, C. Ma, S. Yan, R. Shi, L. Zhang, T. Gao, B. Li, N. Chen, Z. Qiu, An efficient Se-doping strategy to boost sodium storage capacity of anatase TiO2 nanospheres, Scr. Mater. 215 (2022) 114705, https://doi.org/10.1016/j.scriptamat.2022.114705.
[16] D. Sha, Y. You, R. Hu, X. Cao, Y. Wei, H. Zhang, L. Pan, Z. Sun, Revealing the evolution of doping anions and their impact on K-ion storage: a case study of Se-doped In2S3, Energy Storage Mater. 58 (2023) 165–175, https://doi.org/10.1016/j.ensm.2023.03.021.
[17] J. Zhang, Z. Du, T. Yan, F. Zeng, Z. Xu, J. Xu, Z. Meng, X. Hu, J. Zhao, H. Tian, Enhancing redox kinetics by electron orbital modulation for high-performance aqueous energy storage, Energy Storage Mater. 60 (2023) 102831, https://doi.org/10.1016/j.ensm.2023.102831.
[18] Y. Bai, L. Luo, W. Song, S. Man, H. Zhang, C.M. Li, Nitrogen-vacancy-rich VN clusters embedded in carbon matrix for high-performance zinc ion batteries, Adv. Sci. 11 (2024) 2308668, https://doi.org/10.1002/advs.202308668.
[19] Y. Bai, Y. Qin, J. Hao, H. Zhang, C.M. Li, Advances and perspectives of ion-intercalated vanadium oxide cathodes for high-performance aqueous zinc ion battery, Adv. Funct. Mater. 34 (2024) 2310393, https://doi.org/10.1002/adfm.202310393.
[20] J. Xu, X. Gong, Z. Meng, P. Chen, H. Nan, Y. Li, T. Deng, D. Wang, Y. Zeng, X. Hu, H. Tian, Z. Niu, W. Zheng, Bi-interlayer strategy for modulating NiCoP-based heterostructure toward high-performance aqueous energy storage devices, Adv. Mater. 36 (2024) 2401452, https://doi.org/10.1002/adma.202401452.
[21] S. Liu, M. Wang, X. Yang, Q. Shi, Z. Qiao, M. Lucero, Q. Ma, K.L. More, D.A. Cullen, Z. Feng, G. Wu, Chemical vapor deposition for atomically dispersed and nitrogen coordinated single metal site catalysts, Angewandte Chemie Int. Edition 59 (2020) 21698–21705, https://doi.org/10.1002/anie.202009331.
[22] L. Tang, J. Tan, H. Nong, B. Liu, H.-M. Cheng, Chemical vapor deposition growth of two-dimensional compound materials: controllability, material quality, and growth mechanism, Acc. Mater. Res. 2 (2021) 36–47, https://doi.org/10.1021/accountsmr.0c00063.
[23] H. Zhang, Y. Bai, J. Liu, J. Li, Z. Zou, W. Song, W. Sun, C.M. Li, A bean sprout-like cobalt selenium phosphorus nanosheet-composed anode toward fast and high sodium-ion storage, Chem. Commun. 59 (2023) 4794–4797, https://doi.org/10.1039/D3CC00968H.
[24] L. Tan, J. Yu, H. Wang, H. Gao, X. Liu, L. Wang, X. She, T. Zhan, Controllable synthesis and phase-dependent catalytic performance of dual-phase nickel selenides on Ni foam for overall water splitting, Appl. Catal. B: Environ. 303 (2022) 120915, https://doi.org/10.1016/j.apcatb.2021.120915.
[25] Y.-C. Lin, W. Zhang, J.-K. Huang, K.-K. Liu, Y.-H. Lee, C.-T. Liang, C.-W. Chu, L.-J. Li, Wafer-scale MoS2 thin layers prepared by MoO3 sulfurization, Nanoscale 4 (2012) 6637–6641, https://doi.org/10.1039/C2NR31833D.
[26] X. Li, D. Pan, J. Deng, R. Wang, J. Huang, W. Lü, T. Yao, X. Wang, Y. Zhang, L. Xu, Y. Bai, P. Xu, B. Song, Phase-junction engineering boosts the performance of CoSe2 for efficient sodium/potassium storage, J. Mater. Chem. A 9 (2021) 25954–25963, https://doi.org/10.1039/D1TA08072E.
[27] Y. Bai, H. Zhang, H. Song, C. Zhu, L. Yan, Q. Hu, C.M. Li, Engineering anion defects of ternary V-S-Se layered cathodes for ultrafast zinc ion storage, Nano Energy 120 (2024) 109090, https://doi.org/10.1016/j.nanoen.2023.109090.
[28] H. Yang, X. Zhang, W. Li, Y. Chen, X. Tang, Y. Wu, Q. Wei, X. Wang, H. Shu, Construction of Bi-based amorphous/crystalline heterostructures for efficient potassium ion storage, J. Mater. Chem. A 12 (2024) 6093–6102, https://doi.org/10.1039/D4TA00291A.
[29] Y. Yu, H. Zhang, F. Yang, Y. Zeng, X. Liu, X. Lu, Bismuth nanoparticles@carbon composite as a stable and high capacity anode for high-voltage bismuth-manganese batteries, Energy Storage Mater. 41 (2021) 623–630, https://doi.org/10.1016/j.ensm.2021.06.042.
[30] X. Sun, L. Li, S. Jin, W. Shao, H. Wang, X. Zhang, Y. Xie, Interface boosted highly efficient selective photooxidation in Bi3O4Br/Bi2O3 heterojunctions, eScience 3 (2023) 100095, https://doi.org/10.1016/j.esci.2023.100095.
[31] Z.A. Shaikh, N.M. Shinde, P.V. Shinde, S.S. Sangale, S.D. Raut, S.F. Shaikh, S. U. Ekar, M.S. Tamboli, R.S. Mane, Sponge-supported low-temperature chemical synthesis of the hybrid Bi2O3@ppy electrode material for energy-storage devices, Energy & Fuels 37 (2023) 4048–4057, https://doi.org/10.1021/acs.energyfuels.2c03967.
[32] B. He, Y. Ling, Z. Wang, W. Gong, Z. Wang, Y. Liu, T. Zhou, T. Xiong, S. Wang, Y. Wang, Q. Li, Q. Zhang, L. Wei, Modulating selective interaction of NiOOH with Mg ions for high-performance aqueous batteries, eScience 4 (2024) 100293, https://doi.org/10.1016/j.esci.2024.100293.
[33] P. Xiong, J. Wu, M. Zhou, Y. Xu, Bismuth–Antimony alloy nanoparticle@porous carbon nanosheet composite anode for high-performance potassium-ion batteries, ACS. Nano 14 (2020) 1018–1026, https://doi.org/10.1021/acsnano.9b08526.
[34] M. Ahila, M. Malligavathy, E. Subramanian, D.P. Padiyan, Controllable synthesis of α and β-Bi2O3 through anodization of thermally evaporated bismuth and its characterization, Solid. State Ion. 298 (2016) 23–34, https://doi.org/10.1016/j.ssi.2016.10.017.
[35] R. Liu, L. Yu, X. He, H. Liu, X. Ma, Z. Tao, G. Wan, N. Ahmad, B. Peng, L. Shi, G. Zhang, Constructing heterointerface of Bi/Bi2S3 with built-in electric field realizes superior sodium-ion storage capability, eScience 3 (2023) 100138, https://doi.org/10.1016/j.esci.2023.100138.
[36] R. Nagarajan, J. Pandey, P. Kumari, Thorium doped and thorium-carbon co doped metastable β-Bi2O3, Solid. State Sci. 95 (2019) 105938, https://doi.org/10.1016/j.solidstatesciences.2019.105938.
[37] X. Ren, X. He, X. Li, Y. Li, F. Gao, J. Zhang, P. Hu, An optical artificial synapse based on single-crystal Se-vacancy Bi2O2Se, Adv. Opt. Mater. 12 (2024) 2302852, https://doi.org/10.1002/adom.202302852.
[38] G. Yuan, D. Liu, X. Feng, M. Shao, Z. Hao, T. Sun, H. Yu, H. Ge, X. Zuo, Y. Zhang, Situ fabrication of porous CoxP hierarchical nanostructures on carbon Fiber cloth with exceptional performance for sodium storage, Adv. Mater. 34 (2022) 2108985, https://doi.org/10.1002/adma.202108985.
[39] T. Wang, X. Cao, L. Jiao, Ni2P/NiMoP heterostructure as a bifunctional electrocatalyst for energy-saving hydrogen production, eScience 1 (2021) 69–74, https://doi.org/10.1016/j.esci.2021.09.002.
[40] K. Yin, D. Zhou, K. Tan, S. Li, M. Zhao, Q. Lu, C. Teng, X. Lu, A space-confined strategy towards stable α/β-Bi2O3 heterojunction anode for high-energy aqueous battery, J. Colloid. Interface Sci. 651 (2023) 929–937, https://doi.org/10.1016/j.jcis.2023.08.035.
[41] M. Zhao, J. Fu, D. Cai, C. Zhang, B. Fei, Y. Zhang, B. Sa, Q. Chen, H. Zhan, Topological insulator bismuth selenide with a unique cloud-like hollow structure as a bidirectional electrocatalyst for robust lithium–sulfur batteries, J. Mater. Chem. A 11 (2023) 24089–24098, https://doi.org/10.1039/D3TA04930B.
[42] X. Wu, H. Liu, F. Li, L. Lu, W. Li, L. Feng, L. Sun, Exploration of electrocatalytic water oxidation properties of NiFe catalysts doped with nonmetallic elements (P, S, Se), Int. J. Hydrogen. Energy 46 (2021) 38992–39002, https://doi.org/10.1016/j.ijhydene.2021.08.235.
[43] Q. Li, P. Wang, Y. Chen, X. Liao, K.-H. Lam, H. Zhang, Q. Zheng, D. Lin, Rod-like Ni-CoS2@NC@C: structural design, heteroatom doping and carbon confinement engineering to synergistically boost sodium storage performance, J. Colloid. Interface Sci. 664 (2024) 400–408, https://doi.org/10.1016/j.jcis.2024.03.056.
[44] J. Xu, Z. Meng, Z. Hao, X. Sun, H. Nan, H. Liu, Y. Wang, W. Shi, H. Tian, X. Hu, Oxygen-vacancy abundant alpha bismuth oxide with enhanced cycle stability for high-energy hybrid supercapacitor electrodes, J. Colloid. Interface Sci. 609 (2022) 878–889, https://doi.org/10.1016/j.jcis.2021.11.081.
[45] X. Xue, C. Ling, H. Ji, J. Wang, C. Wang, H. Lu, W. Liu, Self-powered and broadband bismuth oxyselenide/p-silicon heterojunction photodetectors with low dark current and fast response, ACS. Appl. Mater. Interfaces. 15 (2023) 5411–5419, https://doi.org/10.1021/acsami.2c15947.
[46] A. Wang, W. Hong, L. Li, R. Guo, Y. Xiang, Y. Ye, W. Deng, G. Zou, H. Hou, X. Ji, Bi3Se4 nanodots in porous carbon: a new anode candidate for fast lithium/sodium storage, Energy Storage Mater. 53 (2022) 1–12, https://doi.org/10.1016/j.ensm.2022.08.042.
[47] Y.-Y. Hsieh, Y.-C. Chuang, H.-Y. Tuan, Unraveling dual mechanisms in quasi-layered Bi2O2Se via defect modulation for high-performance aqueous Zn-ion batteries, Adv. Funct. Mater. 34 (2024) 2406975, https://doi.org/10.1002/adfm.202406975.
[48] H. Yue, M. Han, X. Li, T. Song, Y. Pei, X. Wang, X. Wu, T. Duan, B. Long, Converting commercial Bi2O3 particles into Bi2O2Se@Bi4O8Se nanosheets for "rocking chair" zinc-ion batteries, J. Colloid. Interface Sci. 651 (2023) 558–566, https://doi.org/10.1016/j.jcis.2023.08.034.
[49] Q. Wang, M. Wang, L. Wen, W. Zeng, B. Ge, C. Zhang, Y. Yue, S. Wang, A. New, (De)Intercalation MXene/Bi cathode for ultrastable aqueous zinc-ion battery, Adv. Funct. Mater. 34 (2024) 2214506, https://doi.org/10.1002/adfm.202214506.
[50] Y. Sun, Z. Lian, Z. Ren, Z. Yao, Y. Yin, P. Huai, F. Zhu, Y. Huang, W. Wen, X. Li, R. Tai, D. Zhu, Proton-dominated reversible aqueous zinc batteries with an ultraflat long discharge plateau, ACS. Nano 15 (2021) 14766–14775, https://doi.org/10.1021/acsnano.1c04636.
[51] Q. Deng, F. Liu, X. Wu, C. Li, W. Zhou, B. Long, An aqueous BiI3-Zn battery with dual mechanisms of Zn2+ (de)intercalation and I−/I2 redox, J. Energy Chem. 89 (2024) 670–678, https://doi.org/10.1016/j.jechem.2023.10.035.
[52] L. Peng, X. Ren, Z. Liang, Y. Sun, Y. Zhao, J. Zhang, Z. Yao, Z. Ren, Z. Li, J. Wang, B. Zhu, Y. Gao, W. Wen, Y. Huang, X. Li, R. Tai, K. Yang, D. Zhu, Reversible proton co-intercalation boosting zinc-ion adsorption and migration abilities in bismuth selenide nanoplates for advanced aqueous batteries, Energy Storage Mater. 42 (2021) 34–41, https://doi.org/10.1016/j.ensm.2021.07.015.
[53] C. Xia, J. Guo, Y. Lei, H. Liang, C. Zhao, H.N. Alshareef, Rechargeable aqueous zinc-ion battery based on porous framework zinc pyrovanadate intercalation cathode, Adv. Mater. 30 (2018) 1705580, https://doi.org/10.1002/adma.201705580.
[54] L. Wen, Q. Zhang, J. Shi, F. Wang, S. Wang, Z. Chen, Y. Yue, Y. Gao, Layered topological insulator MnBi2Te4 as a cathode for a high rate performance aqueous zinc-ion battery, ACS. Nano 18 (2024) 5981–5990, https://doi.org/10.1021/acsnano.4c01137.
[55] K. Guo, W. Cheng, Z. Li, Y. Wan, H. Wang, Y. Li, X. Zhong, N. Yu, V2O4·2H2O nanocrystal as a novel cathode material for aqueous zinc ion batteries, J. Alloys. Compd. 972 (2024) 172719, https://doi.org/10.1016/j.jallcom.2023.172719.
[56] K. Guo, Y. Li, D. Luo, Y. Guo, S. Pan, S. Lin, N. Yu, Room-temperature synthesis of VO(OH)2 as a high capacity cathode material for aqueous zinc ion batteries, J. Alloys. Compd. 1004 (2024) 175772, https://doi.org/10.1016/j.jallcom.2024.175772.

[57] K. Guo, W. Cheng, H. Liu, W. She, Y. Wan, H. Wang, H. Li, Z. Li, X. Zhong, J. Ouyang, N. Yu, Sn-doped hydrated V2O5 cathode material with enhanced rate and cycling properties for zinc-ion batteries, Crystals. (Basel) 12 (2022), https://doi.org/10.3390/cryst12111617.
[58] K. Guo, W. Cheng, H. Chen, H. Li, J. Chen, H. Liu, Y. Tu, W. She, Z. Huang, Y. Wan, L. Zou, Z. Li, X. Zhong, Y. Wu, X. Wang, N. Yu, Facile and rapid synthesis of porous hydrated V2O5 nanoflakes for high-performance zinc ion battery applications, Nanomaterials 12 (2022), https://doi.org/10.3390/nano12142400.
[59] M. Xu, S. Gong, Y. Niu, K. Zhang, T. Liu, Z. Chen, Bismuth-based metal-organic frameworks derived rod-like nanoreactors for neutral aqueous battery-type anode, Sci. China Mater. 66 (2023) 106–117, https://doi.org/10.1007/s40843-022-2117-x.
[60] X. Cui, Y. Li, Y. Zhang, Z. Sun, Y. Liu, J. Zhang, E. Xie, J. Fu, Unraveling the electrochemical charge storage dynamics of defective oxides-based cathodes toward high-performance aqueous zinc-ion batteries, Chem. Eng. J. 478 (2023) 147197, https://doi.org/10.1016/j.cej.2023.147197.
[61] J.S. Ko, C.-H. Lai, J.W. Long, D.R. Rolison, B. Dunn, J.N. Weker, Differentiating double-layer, psuedocapacitance, and battery-like mechanisms by analyzing impedance measurements in three dimensions, ACS. Appl. Mater. Interfaces. 12 (2020) 14071–14078, https://doi.org/10.1021/acsami.0c02020.